Article

Highly stable perovskite solar cells with 0.30 voltage deficit enabled by a multi-functional asynchronous cross-linking

Qiong Liang[1], Kuan Liu [1,2] ✉, Yu Han[1], Hao Xia[1], Zhiwei Ren [1], Dongyang Li [1], Tao Zhu[1], Lei Cheng[1], Zhenrong Wang[1], Cheng Zhu [3], Patrick W. K. Fong [1], Jiaming Huang[1], Qi Chen [3], Yang Yang [4] ✉ & Gang Li [1,2,5] ✉

The primary challenge in commercializing perovskite solar cells (PSCs) mainly stems from fragile and moisture-sensitive nature of halide perovskite materials. In this study, we propose an asynchronous cross-linking strategy. A multifunctional cross-linking initiator, divinyl sulfone (DVS), is firstly pre-embedded into perovskite precursor solutions. DVS, also as a special co-solvent, facilitates intermediate-dominated perovskite crystallization manipulation, favouring formamidine-DVS based solvate transition. Subsequently, DVS-embedded perovskite as-cast films are post-treated with a nucleophilic reagent, glycerinum, to trigger controllably three-dimensional co-polymerization. The resulting cross-linking scaffold provides enhanced water-resistance, releases residual tensile strain, and suppresses deep-level defects. We achieve a maximum efficiency over 25% (certified 24.6%) and a maximum V_{OC} of 1.229 V, corresponding to mere 0.30 V deficit, reaching 97.5% of the theoretical limit, which is the highest reported in all perovskite systems. This strategy is generally applicable with enhanced efficiencies approaching 26%. All-around protection significantly improves PSC's operational longevity and thermal endurance.

Photovoltaic (PV) technology has shown great potential in offering a clean and sustainable solution to the issue of global energy scarcity. The interest in organic-inorganic hybrid perovskite materials has been growing rapidly due to their advantageous characteristics, such as high charge carrier mobility and lifetime, tuneable bandgaps, high absorption coefficient, and good solubility in common polar aprotic solvents[1–3]. These materials have been widely used in various optoelectronic and electronic applications, including solar cells, light-emitting devices, lasers, and photodetectors. Among them, solar cells based on organic-inorganic halide perovskites (OIHPs) have emerged as a leading technology in the field of emerging photovoltaics, which is comparable with market leader crystalline silicon, gallium arsenide (GaAs), copper indium gallium selenide (CIGS), cadmium telluride (CdTe) technologies and so on.

The intrinsic stability of the perovskite layer and key interfaces remains the primary challenge in the commercialization of perovskite solar cells (PSCs), despite the significant advancements in laboratory-scale PSCs, achieving certified power conversion efficiency (PCE) over 26%[4]. This challenge mainly arises from the fragile and ionic nature of halide perovskite materials, which make them highly sensitive and reactive toward the ambient environment[5–7]. Solution deposition of perovskite thin films would spontaneously induce high concentrations

[1]Department of Electrical and Electronic Engineering, The Hong Kong Polytechnic University, Hung Hom, Kowloon, Hong Kong, China. [2]Research Institute for Smart Energy (RISE), The Hong Kong Polytechnic University, Hung Hom, Kowloon, Hong Kong, China. [3]Advanced Research Institute of Multidisciplinary Science, Beijing Institute of Technology, Beijing 100081, China. [4]Department of Materials Science and Engineering, California NanoSystems Institute, University of California Los Angeles, Los Angeles, CA, USA. [5]Photonics Research Institute (PRI), The Hong Kong Polytechnic University; Hung Hom, Kowloon, Hong Kong, China. ✉e-mail: kuan-lk.liu@polyu.edu.hk; yangy@ucla.edu; gang.w.li@polyu.edu.hk

of intrinsic defects (e.g., halide vacancies, under-coordinated lead cations) at perovskite surface and grain boundaries (GBs). Such defects are likely to be detrimental to the device performance (especially open-circuit voltage, V_{OC}) and would accelerate the perovskite degradation under ambient atmosphere, especially humidity[8]. It's well recognized that delicate control of perovskite formation and crystallization kinetics (nucleation and crystal growth rate), as well as various passivation strategies, are of great significance to mitigate the perovskite defects issue to a great extent[9,10].

The interfacial strain caused by lattice distortion of the microscopic perovskite crystal structure directly affects its optoelectronic properties and accelerates perovskite degradation as well. Strain engineering has been developed as an advanced approach to further enhance the performance (e.g., V_{OC}) and operational stability of devices[11]. So far, this field is still lacks of reports reaching 95% of the S-Q limit in V_{OC}. The soft and elastic nature of polymer is highly valuable in regulating residual strain during perovskite formation, and provides intrinsic moisture resistance[12-14]. Whereas, due to strong coordinate interaction with perovskite precursors, polymer-based complexes are easy to precipitate from perovskite solutions when incorporated in large amounts for regulation[15-17]. An alternative approach is to incorporate cross-linkable ligands into perovskite precursor solutions or through an antisolvent technique and trigger in-situ polymerization under the stimulus of thermal or ultraviolet during or after the solidification of perovskite films[18-20]. So far, most related works synchronously fed monomers into perovskites and induced spontaneous but uncontrollable polymerization, which might cause uncertainty of perovskite precursor stoichiometry and colloidal size, thus disrupting the delicate perovskite crystallization process. There is a lack of synergy works that implement delicate perovskite crystallization manipulation and provide all-around protection of perovskites.

In this work, we demonstrate an asynchronous incorporation of cross-linkable agents to trigger a controllable co-polymerization at perovskite surface and GBs (Fig. 1a). We first pre-embed an effective cross-linking initiator, divinyl sulfone (DVS), into perovskite precursor solutions. As a co-solvent with low coordination ability (low donor number, DN), DVS facilitates the intermediate-dominated perovskite crystallization manipulation through a favourable FAI-DVS-based solvate transition, while maintaining the kinetic balance between perovskite nucleation and crystal growth, and thus delivering high-quality perovskite films with low defect density. More importantly, the pre-embedded cross-linking initiator triggers three-dimensional co-polymerization into a controllable macro reticular structure, through a post-treated nucleophilic reagent, glycerinum (gly) upon the as-cast perovskite films. The resulting co-polymer scaffold not only effectively passivates the intrinsic defects at the perovskite surface and GBs, but also releases the residual tensile strain at the near-surface region. As a result, we achieve a maximum PCE of 25.22% (certified 24.6%) with a maximum V_{OC} of 1.229 V, corresponding to a mere 0.30 V deficit (for bandgap of ~1.53 eV, coincident with the measured nonradiative recombination loss of only 52.5 mV from EQE_{EL}), reaching 97.5% of the theoretical S-Q V_{OC} limit, which is the highest reported in all perovskite systems. This strategy is generally applicable across perovskite compositions and device architectures, delivering a promising PCE of 25.98% for p-i-n structured devices. All-around co-polymerization significantly enhances the moisture resistance of perovskite films and devices and achieves enhanced operational stability at elevated temperature (ISOS-L-3: MPP, 65 °C, 50% RH, $T_{98} = 1350$ h) and room temperature (ISOS-L-1: MPP, 60% RH, $T_{90} = 1800$ h), as well as thermal stability in dark (ISOS-D-2I: 85 °C, N_2, $T_{95} = 1560$ h).

Result
Divinyl Sulfone Characteristics
The cross-linking initiator, DVS, was firstly incorporated into perovskite precursor solution as a co-solvent and mixed with the main solvent DMF in an appropriate volume ratio (0 to 20%, v:v). The
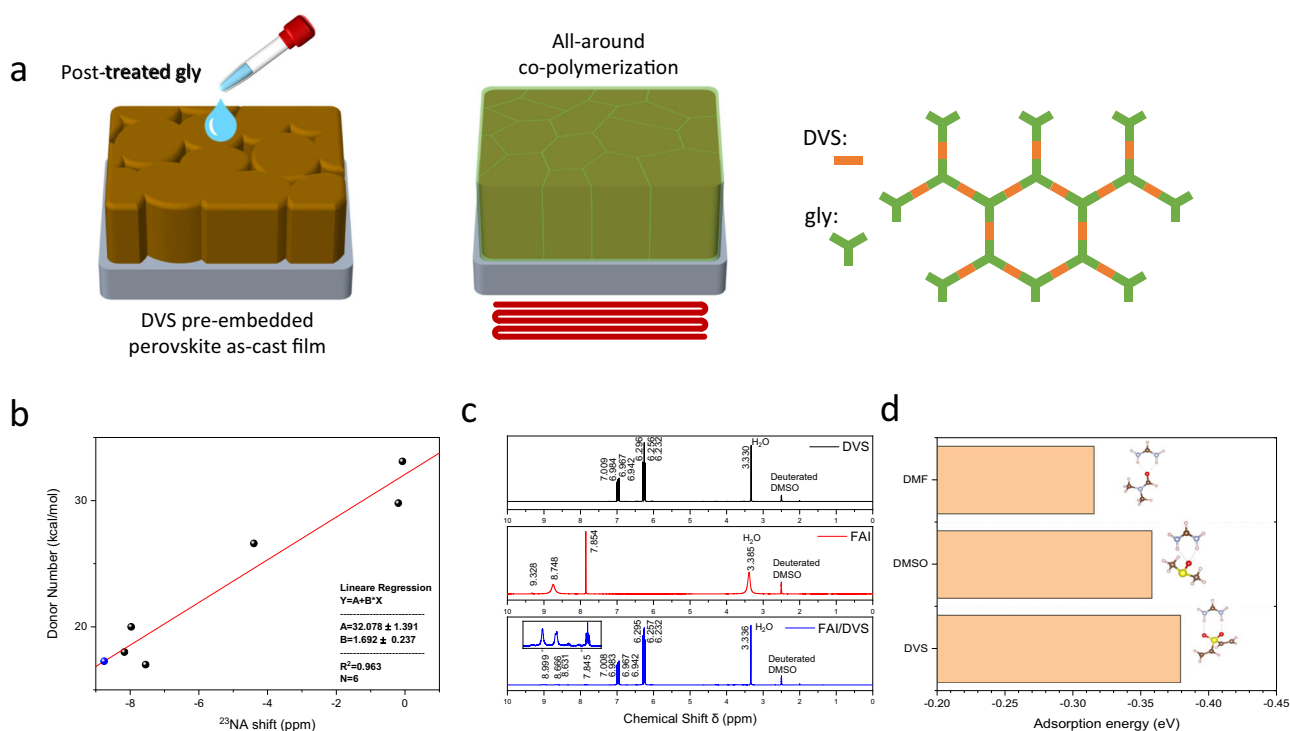
Fig. 1 | Asynchronous Cross-linking Illustration and Divinyl Sulfone Characteristic. a Schematic illustration of intermediate-dominated perovskite crystallization by pre-embedded DVS and all-around co-polymerization protection through the post-treatment of gly. **b** Linear fitting of ^{23}Na NMR chemical shift and DN of the selected organic solvents to calculate the DN of DVS. **c** 1H NMR spectra of FAI, DVS, and FAI/DVS into DMSO-d6 solution, respectively. **d** DFT calculation of adsorption energy of FA+ with different solvents.

conventional solvent system (DMF/DMSO = 5:1, v:v) was used for comparison. It should be noted that the crystallization kinetics of perovskite film is not only determined by the boiling point, viscosity, and vapour pressure of solvent systems but also highly affected by the coordinate chemistry within the perovskite ink, as well as the intermediate phase transition.

Donor number (DN) is a quantitative measurement of the Lewis basicity of a solvent that evaluates its coordinate interaction with Lewis acid (e.g., PbI_2)[21]. In order to study the precursor chemistry within the DVS-based solvent system, we first examined the DN of DVS by ^{23}Na nuclear magnetic resonance (NMR) spectroscopy. A series of common organic solvents were selected with reported DN values (Supplementary Table 1) to facilitate the study. An appropriate amount of $NaClO_4$ was dissolved into these solvents to prepare a 0.2 M solution. The DN of DVS was extracted from the linear fitting against ^{23}Na NMR shift to be 17.3 kcal/mol (Fig. 1b, Supplementary Fig. 1, Supplementary Table 1), much lower than the commonly used aprotic organic solvents (e.g., DMSO).

As a result, DVS is a low Lewis basic solvent, which exhibits weak coordinate interaction with PbI_2 (Supplementary Fig. 2). In contrast, there is a strong interaction between DVS and ammonium iodide (e.g., FAI). We dissolved FAI into DVS delivering a clear solution but with a different colour compared with the DVS solvent (Supplementary Fig. 2). When X-ray diffraction (XRD) spectroscopy was performed on the quasi-wet film using FAI in DVS solution, we observed additional diffraction peaks at $2\theta = 12.78°$ and $14.19°$ besides the characteristic peaks of FAI powder (Supplementary Fig. 3), which may indicate an additional solvate phase based on FAI-DVS. ^1H NMR result also verifies this chemical interaction (Fig. 1c). The hydrogen chemical shifts are located at 7.854 and 8.748 ppm for pure FAI solution, whereas, in FAI/DVS solution, we observe a notable shift and split of the hydrogen signals at 7.845, 8.631 and 8.666 ppm, implying different chemical environment and a strong chemical interaction between DVS and FA^+.

To further elucidate the solute-solvent interaction, we performed density function theory (DFT) calculation for the adsorption energy of FA^+ with DMF, DMSO, and DVS, respectively (Supplementary Fig. 4-5, and Supplementary Table 2, also see computation details in Supplementary Note 1)[22]. Compared with these current standard solvents, FA^+ exhibited the largest adsorption energy with DVS, as shown in Fig. 1d, agreed well with our experimental results. We also conducted ab initio molecular dynamics (MD) to understand the solvation effects at the pre-nucleation stage of perovskite precursor solutions. We performed ~20 ps MD simulation to evaluate the precursor-solvent mixtures evolution in two co-solvent systems (DMF/DMSO and DMF/DVS, see computation details in Supplementary Note 1). As shown in Fig. 2a, we find that both Pb^{2+} and ammonium cations (FA^+ and MA^+) are highly coordinated with oxygen atoms in DMSO, thus forming individual small-size Pb-I clusters in DMF/DMSO system. However, in DMF/DVS system, we find that more large-size Pb-I clusters of edge-sharing iodoplumbate start to form during the MD simulations (Fig. 2a and Supplementary Fig. 6), which can be also expected due to the weak bonding between DVS and PbI_2 (low DN). These Pb-I clusters can act as nucleation centers to further facilitate nucleation of perovskite nanocrystals. One of the main insights from this MD simulation is that there are additional functional co-solvents for DMF, like DVS, that can be used to tune the solvent-solute interaction, with a direct impact on the subsequent perovskite nucleation and crystallization kinetics, as will be discussed below[23].

Crystallization Dynamics in Intermediate Complex and Perovskite Formation

To provide a comprehensive insight into the perovskite crystallization kinetics affected by the DVS pre-embedded precursor solution, we analysed the time-resolved UV-vis absorption spectroscopy during the antisolvent-assisted spin-coating process. Figure 2b shows the two-dimensional pseudo-colour absorption intensity mapping as a function of spin-coating time. We dripped chlorobenzene (CB) upon the surface of perovskite wet film during spin coating (at 25 s) and found the sample from DVS-based perovskite ink (DMF/DVS = 5:1, v:v) shows much faster nucleation kinetics compared to that from DMSO-based ink (DMF: DMSO = 5:1, v:v) (Supplementary Fig. 7), coincident well with the result from MD simulation. The as-cast perovskite films were then treated with gly to trigger co-polymerization at the perovskite surface and GBs during thermal annealing. We used the same technique to measure the perovskite crystal growth rate in this process quantitively. Figure 2c shows the pseudo-colour mapping of the in situ UV-vis absorption spectra as a function of annealing time. We performed the first derivative of absorbance at 450 nm versus time and calculated the average perovskite crystal growth rates to be 0.073 and $0.061 s^{-1}$, respectively, for the control and DVS-gly based perovskite films (Supplementary Fig. 8).

We further performed a detailed diagnosis of phase transitions that occurred during the thermal annealing process, using in-situ XRD spectroscopy between the control and DVS-gly-based samples. For the as-cast control sample, besides the characteristic diffraction peaks of cubic $FAPbI_3$ at $2\theta = 14.01°$, $19.88°$, $24.39°$, and $28.24°$, corresponding to (001), (011), (111) and (002) planes, we observed the signal related solvates at $2\theta < 10°$ (Supplementary Fig. 9a). For comparison, the as-cast DVS-based perovskite film shows two distinct diffraction peaks at $2\theta = 11.51°$ and $24.05°$, which gradually vanish along with thermal annealing (Figs. 2d, 2e, and Supplementary Fig. 9b). This signal is likely ascribed to the FAI-DVS solvate, which confirms that cubic perovskite nanocrystals and additional FA-based intermediate complex transition co-exist in the DVS-based sample. We extracted the XRD intensity of the perovskite main peak at $2\theta = 14.01°$ as a function of annealing time, as shown in Fig. 2f. There is a pronounced delay of perovskite-crystal growth for the DVS-gly-based sample, which is mainly due to the necessary thermal energy to dissociate the intermediate and recrystallize into the cubic perovskite phase, as well as to induce the co-polymerization. It has been well recognized that delayed crystal growth is favoured to form high-quality perovskite films with better crystallinity, more dominated grain orientation, and lower defect density[24].

Cross-linking and Defects Passivation

Cross-link reaction between the pre-embedded initiator (DVS) and post-treated nucleophilic reagent (gly) was confirmed through Fourier transform infrared spectroscopy (FTIR) and matrix-assisted laser desorption/ionization time-of-flight mass spectrometry (MALDI-TOF-MS). In FTIR, the characteristic signal of DVS with the C−C stretching vibration of vC = C at $1610 cm^{-1}$ was diminished after thermal annealing, while a distinct peak corresponding to the stretching vibration of C-O-C at $1275 cm^{-1}$ and $830 cm^{-1}$ appeared (Fig. 3a, and Supplementary Fig. 10b)[25,26]. This result validates the high reactivity in nucleophile-mediated oxa-Michael addition reactions between DVS and gly (Supplementary Fig. 11)[27]. It should be noted that this addition reaction is the sole pathway for the controllable co-polymerization into the macro reticular structure. Furthermore, the characteristic peaks of S = O at 1310 and $1132 cm^{-1}$ are displayed in both the as-cast and post-treated samples, confirming the existence of DVS-gly co-polymer in final perovskite after thermal annealing (Supplementary Fig. 10a). MALDI-TOF-MS was further performed to examine the cross-link reaction, which verifies the presence of a few fragments in the DVS-gly network (Fig. 3b, details in Supplementary Note 2). The degree of co-polymerization could be delicately controlled by the molar ratio between gly and DVS, measured by gel permeation chromatography (details in Supplementary Note 3, Supplementary Fig. 12, and Supplementary Table 3).

After the controllable co-polymerization and perovskite crystal growth, the control, DVS, and DVS-gly-based perovskite films showed
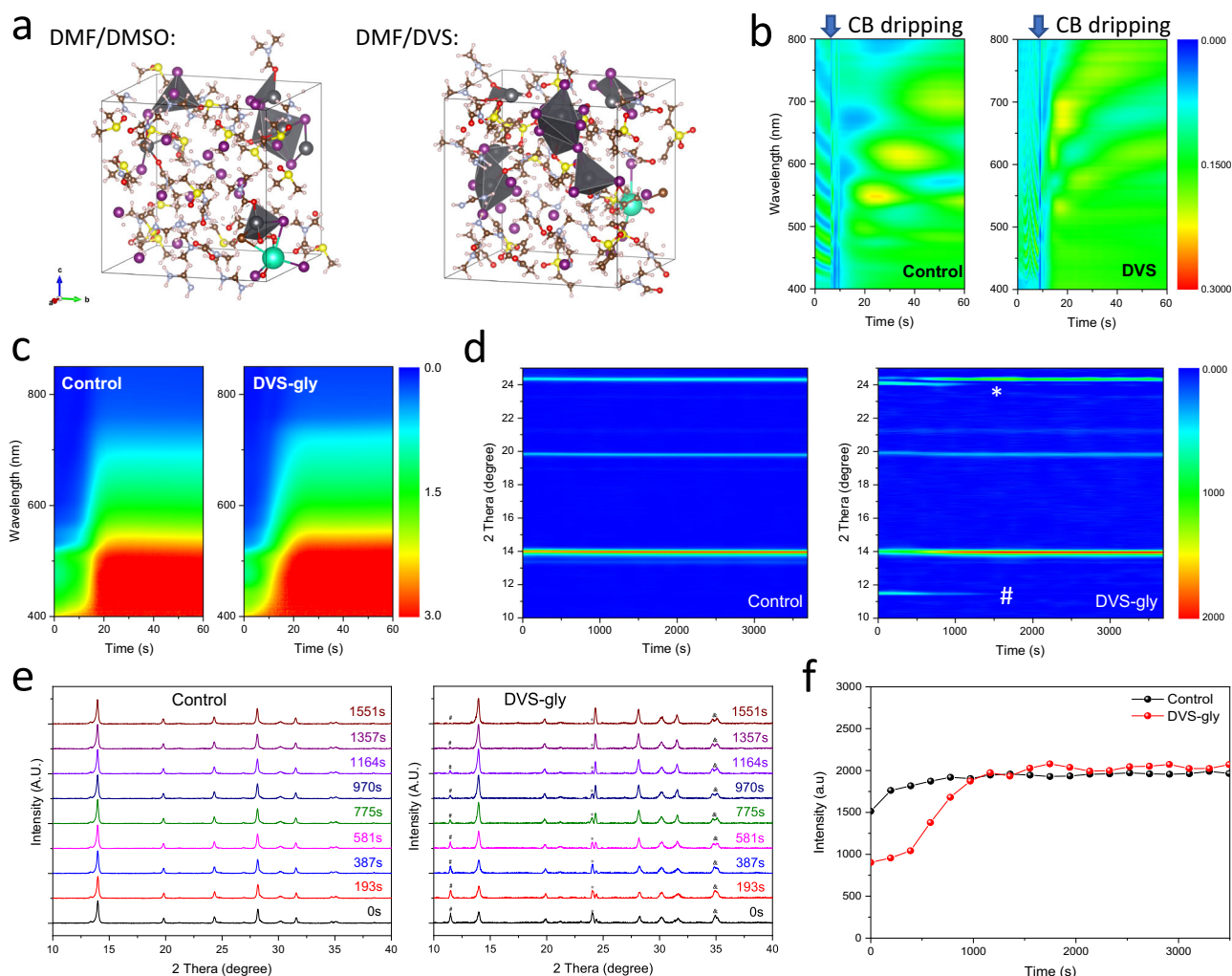
Fig. 2 | Crystallization Dynamics in Intermediate Complex and Perovskite Formation. a Ab initio MD simulations of perovskites precursors in DMF/DMSO and DMF/DVS solvent systems after ~20 ps, in which iodoplumbate polyhedra are shown within 4 Å cutoff. **b** Two-dimensional pseudo-colour absorption intensity mapping as a function of spin-coating time during the in-situ measurement. **c** Pseudo-colour mapping of the UV-vis absorption spectra as a function of annealing time. **d** In-situ XRD measurement of the control and DVS-gly based perovskite films during thermal annealing (intermediate phases presented by # and * symbol can be ascribed to FAI-DVS solvate). **e** Corresponding XRD spectra as a function of annealing time. **f** XRD intensity evolution of the perovskite main peak at $2\theta = 14.01°$.

identical XRD patterns, and no low-dimensional perovskites or non-perovskites were detected (Supplementary Fig. 13a), corresponding to the characteristic diffraction peaks of cubic FAPbI$_3$, which may indicate that the DVS-gly co-polymer scaffold distributes at perovskite surface and GBs. Among them, the DVS-gly-based perovskite film exhibits the sharpest XRD patterns, with the full width at half maximum (FWHM) of (100) narrowed down from 0.231° (control) to 0.193°, indicating better crystallinity (Supplementary Fig. 13b). Top-view scanning electron microscopy (SEM) image of DVS-gly based perovskite film displays a homogenous and compact grain, with slightly enlarged GBs (Supplementary Fig. 14), which validates that the DVS-gly scaffold was mainly constructed at perovskite GBs during thermal annealing.

It's well known that the lattice mismatch mainly arises from unfavoured phase transition and perovskite grain propagation, inducing the residual strain and intrinsic defects in final perovskite films and eventually accelerating perovskite degradation[18]. Here, we performed depth-dependent grazing incident X-ray diffraction (GI-XRD) in $2\theta-\sin^2\psi$ mode to identify the lattice mismatch and analyse the evolution of residual strain across the perovskite film through varying grazing incident angles (Figs. 3c and d). The nearly equivalent depth-dependent XRD patterns show that the film had the same cubic phase

structure at each depth. We selected two typical regions (50 nm at near perovskite surface and 200 nm in bulk) by varying the appropriate instrument angles (Supplementary Table 4). The (012) plane at $2\theta = 31.6°$ is characteristic for strain analysis due to its high multiplicity, which is generally adopted to acquire more grain information and alleviate the orientation effect on the linear relationship of $2\theta-\sin^2\psi$ in this method[28]. For the control sample, we observed a pronounced shift of (012) peak to the smaller 2θ along with the increase of instrument tilt angle ψ, which indicates an increase of crystal plane distance $d_{(012)}$ and thus the tensile strain bears at the near-surface region (Fig. 3c). In comparison, the position of the (012) peak almost remained unchanged for the DVS-gly based perovskite, which suggests that the soft nature of DVS-gly co-polymer scaffold could effectively diminish the uneven distribution of residual tensile strain at the near-surface region (Fig. 3d). We observed the same function for the DVS-gly sample in the bulk region (Supplementary Fig. 15), which implies the co-polymer network may penetrate through the whole thickness of perovskite film. In-depth element analysis using X-ray photoelectron spectroscopy (XPS) was further performed to prove that the DVS-gly co-polymer was uniformly distributed across the whole perovskite film, with constant characteristic signals of S and O element within 500 s etching (Fig. 3e).
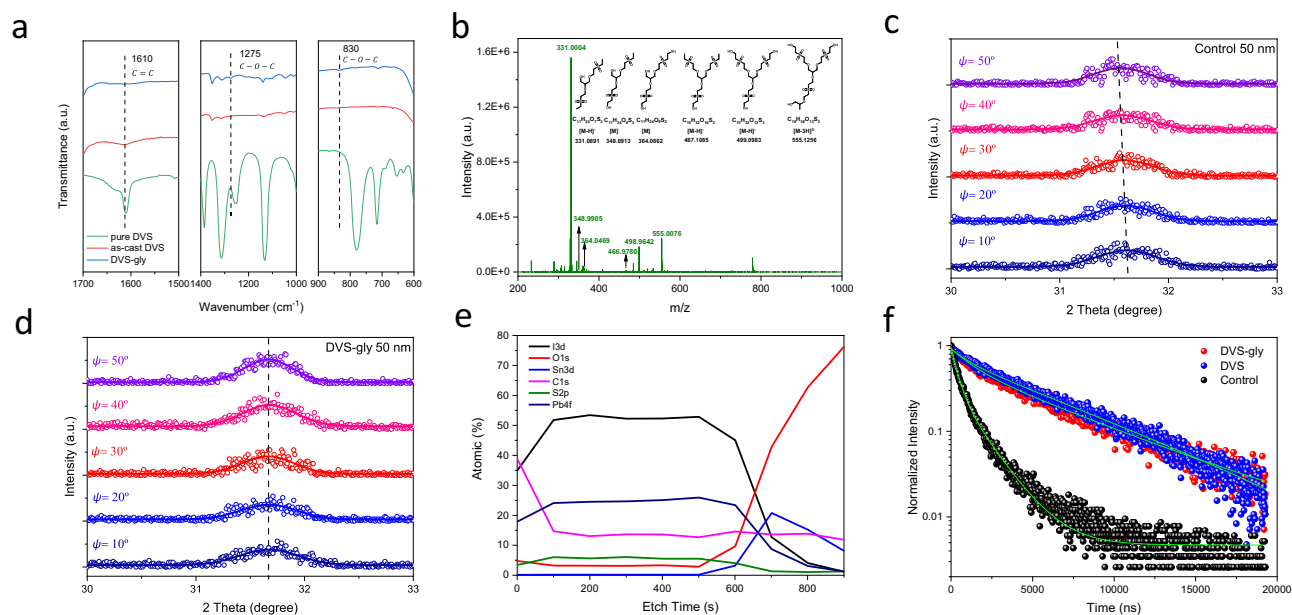
Fig. 3 | Cross-linking and defects passivation. a FITR spectra in selected region for the DVS solvent, as-cast DVS-based perovskite film, and DVS-gly based perovskite final film after annealing. **b** MALDI-TOF-MS measurement for the DVS/gly mixture solution. **c**–**d** GI-XRD spectra in $2\theta-\sin2\psi$ mode for (**c**) control and (**d**) DVS-gly based perovskite films at near surface region (50 nm depth), respectively. **e** In-depth XPS spectra for the DVS-gly-based perovskite film. **f** TRPL decay for the control, DVS, and DVS-gly based perovskite films.

These results imply that our strategy provides all-around protection at perovskite surface and GBs.

Steady-state and time-resolved photoluminescence (TRPL) spectra were conducted to explore the charge recombination behaviour in the perovskite films. The DVS-gly-based perovskite on glass substrate shows a much more pronounced and slightly blue-shifted PL peak (805 nm), compared with the control perovskite film (809 nm), which is a sign of a reduced trap density of state (tDOS) near the band tail (Supplementary Fig. 16). TRPL decay spectra were fitted using the bi-exponential function, and the fitting parameters are summarized in Supplementary Table 5. It should be noted that the excitation fluence in our study is very low (636.2 nm, ≤ 5 nJ/cm^2), which only generates a much lower density of free carriers (2.4×10^{14} cm^{-3}, much lower than the trap density) compared with that of trap states[29]. In this condition, TRPL decay mainly responds to the trap-assisted recombination behaviour in the bulk perovskite. Compared with the control sample (782.88 ns), the DVS and DVS-gly-based samples show a much pro-longed lifetime on average (4091.66 and 4682.63 ns, respectively), which indicates that this strategy significantly reduces non-radiative recombination both through the delicate crystallization manipulation and effective passivation by the co-polymer network (Fig. 3f).

Device Performance

We fabricated the conventional n-i-p PSCs assembled with the structure of FTO/TiO$_2$/SnO$_2$ QDs/perovskite/spiro-OMeTAD/Au, using the perovskite ink mixed with an appropriate amount of DVS (0 to 20%, v:v, regarding the main solvent DMF). We first examined the work functions of the corresponding perovskite films using ultraviolet photoemission spectroscopy (UPS), as shown in Supplementary Fig. 17. These samples display a downward trend of work functions (-4.513, -4.629, and -4.691 eV for control, DVS, and DVS-gly-based perovskite films, which may relate to the relief of negatively charged iodine interstitial (I$_i^-$) defects[30]. Supplementary Fig. 18 shows the J-V curves of the best-performance devices under different volume ratios of DVS, and Supplementary Table 6 summarizes their photovoltaic characteristics. Along with the volume ratio DVS from 0 to 20%, V$_{OC}$ values exhibit an increasing trend from 1.200 to 1.229 V. At the same

time, J$_{SC}$ almost keeps constant at ~25.2 mA cm^{-2}, which is well agreed with the integrated value from external quantum efficiency (EQE) spectra (Fig. 4b, less than 3% mismatch). Among them, devices from the ink with 7% DVS deliver the highest efficiency, with a maximum PCE of 25.08%. We kept the optimized conditions of DVS unchanged, and further investigated the concentration dependence of gly post-treatment on performance (molar ratio of gly versus DVS, from 4.3 to 64 mol%) as shown in supplementary Fig. 19 and Supplementary Table 7. At 32 mol% gly post-treatment, we delivered the highest efficiency for DVS-gly based devices, up to 25.22% (certified 24.63%), as illustrated in Fig. 4a and Supplementary Fig. 20. Table 1 shows the photovoltaic parameters of the control, DVS-based, and DVS-gly-based PSCs under optimized conditions.

Moreover, these devices have demonstrated a maximum V$_{OC}$ of 1.229 V (Fig. 4c). Photovoltaic bandgap (Eg^{IP}) of the FA-dominated perovskite used in this work was calculated to be 1.53 eV from the first differential of EQE spectra (Supplementary Fig. 22). As far as we known, 1.229 V V$_{OC}$ is the highest reported value in this bandgap of perovskite, and the corresponding V$_{OC}$ deficit (0.301 V) is the lowest among all perovskite systems (Supplementary Table 8). It is noteworthy that the V$_{OC}$ of our devices reached 97.5% of the theoretical V$_{OC}$ limit, as demonstrated in Fig. 4d. We also validated this strategy on p-i-n structured devices, based on different perovskite compositions, deli-vering a maximum PCE of 25.98% with enhanced V$_{OC}$ (Supplementary Fig. 23 and Supplementary Table 9). When upscaling the device area, we achieved the maximum PCE of 21.75% for the minimodule (3-sub-cells, 3.6*3.6 cm^2 substrate, Supplementary Fig. 24).

By quantifying the dominated recombination mechanisms, we uncover the increase of V$_{OC}$ in DVS-gly-based devices using the elec-troluminescence method. We measured the external quantum effi-ciency of electroluminescence (EQE$_{EL}$) when a PSC operating as a light-emitting diode (LED) in forward voltage bias (Fig. 4e and Supplemen-tary Fig. 25). The non-radiative recombination loss (ΔV$_{OC,nr}$) can be derived from the EQE$_{EL}$ at the injection current density equal to J$_{SC}$[31]. Compared with the control device (EQE$_{EL}$ = 1.28%, ΔV$_{OC,nr}$ = 113 mV), The DVS-gly device exhibits a much enhanced EQE$_{EL}$ of 13.11% at injection current density equal to J$_{SC}$, corresponding to a ΔV$_{OC,nr}$ of

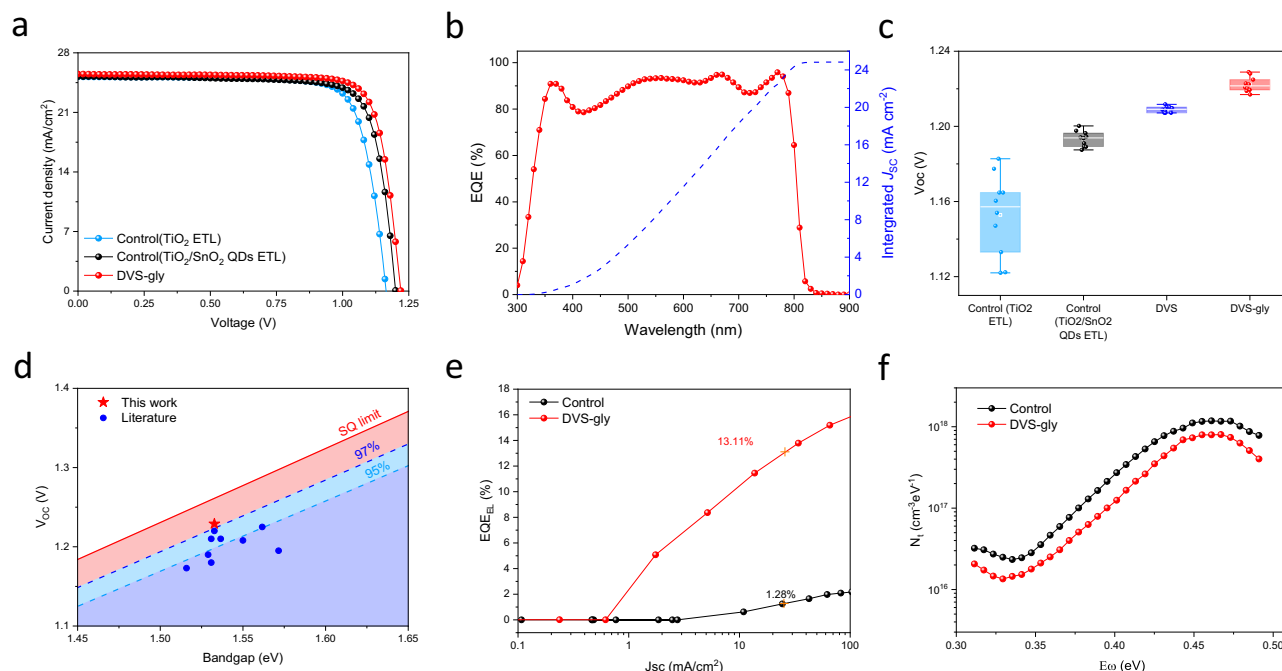**Fig. 4 | Device Performance. a** J-V curves of the best-performance control (TiO$_2$ ETL), control (TiO$_2$/SnO$_2$ QDs ETL), and DVS-gly-based devices. **b** EQE spectrum of the DVS-gly-based PSCs. **c** V$_{OC}$ distribution of the control (TiO$_2$ ETL), the control (TiO$_2$/SnO$_2$ QDs ETL), 7% DVS and DVS-gly based devices. **d** Comparison of the V$_{OC}$ with different bandgaps of PSCs from the literature to our work (**e**) EQE$_{EL}$ as a function of the injection current density to calculate the nonradiative recombination loss. **f** Energetic distribution of trap density for the control and DVS-gly based PSCs measured by admittance spectroscopy.

52.5 mV, coincident with the V$_{OC}$ deficit from J-V test. The V$_{OC}$ deficit was also validated by QFLS analysis (detail see Supplementary Note 4, Supplementary Fig. 26, and Supplementary Table 10). This result indicates the hybrid asynchronous cross-linking significantly suppresses the non-radiative recombination at perovskite surface and GBs, which dominates the V$_{OC}$ enhancement for the DVS-gly-based devices.

Thermal admittance spectroscopy (TAS) was further performed to quantitatively estimate the energetic distribution of trap density of states (tDOS) under an AC voltage with the frequency decreased from 10^6 to 100 Hz[32]. Compared with the control device (N$_t$ = 8.33 × 10^{16} cm^{-3}), the DVS-gly-based devices display much lower trap density (N$_t$ = 5.09 × 10^{16} cm^{-3}) (Fig. 4f). It's well known that deep defects (>0.35 eV here) at perovskite surface and GBs are mainly regarded as the nonradiative recombination center, which is significantly detrimental to the V$_{OC}$ of PSCs[33]. DVS-gly strategy not only manipulates the delicate crystallization process through the favoured intermediate-dominated transition, delivering high-quality perovskite crystal but also relieves these intrinsic defects via the controllable co-polymerization at perovskite surface and GBs efficiently. Our strategy synergistically eliminates the intrinsic deep defects to a great extent and pushes the V$_{OC}$ value close to the radiative limit.

To further study the charge transport/recombination behaviour in PSCs, we performed electrochemical impedance spectroscopy (EIS)[34]. Supplementary Fig.. 27a and b show Nyquist plots for the control and DVS-gly-based devices under AC bias frequency from 10^6 to 100 Hz, respectively. The equivalent circuit for simulating charge transfer and recombination is shown in the inset, where R$_S$ is the series resistance of the devices, and R$_{rec}$ is the recombination resistance in the bulk perovskite, inversely related to the rate at which photo-generated carrier recombination. The DVS-gly devices show lower R$_S$ than that of the control devices, which is highly related to the enhanced FF measured by J-V curves (Supplementary Fig. 27c). More importantly, the higher R$_{rec}$ for the DVS-gly devices is mainly responsible for the reduced recombination rate of photogenerated carriers in the bulk perovskite (Supplementary Fig. 27d), which is in accordance with the enhanced V$_{OC}$ as mentioned before.

Perovskite Film Water Resistance and Device Stability

In addition to the device performance, the long-term stability under various aging conditions, especially the long-term operational stability, is of great significance for the future commercialization of PSC technology. The DVS-gly co-polymerization strategy provided enhanced moisture resistance to the perovskite films through inner encapsulation (Figs. 5a and b, Supplementary Movies 1 and 2). Compared to the control perovskite film which turns yellow immediately, while, the DVS-gly protected perovskite film kept black even after 180 s in water. The unencapsulated DVS-gly-based perovskite devices also exhibit much-improved stability directly under water soaking (Supplementary Table 11).

For long-term stability, we monitored the PCE evolution for the control and DVS-gly based devices under MPP tracking and continuous 1-sun illumination at elevated temperature (ISOS-L-3: 65 ± 5 °C, 50 ± 5% RH, PTAA-based n-i-p devices) and room temperature (ISOS-L-1: 30 ± 5 °C, 60 ± 5% RH, spiro-OMeTAD based n-i-p devices), respectively. DVS-gly based devices maintained over 98% of their initial PCE after 1350 h operation at 65 °C, and 90% after 1800 h operation at
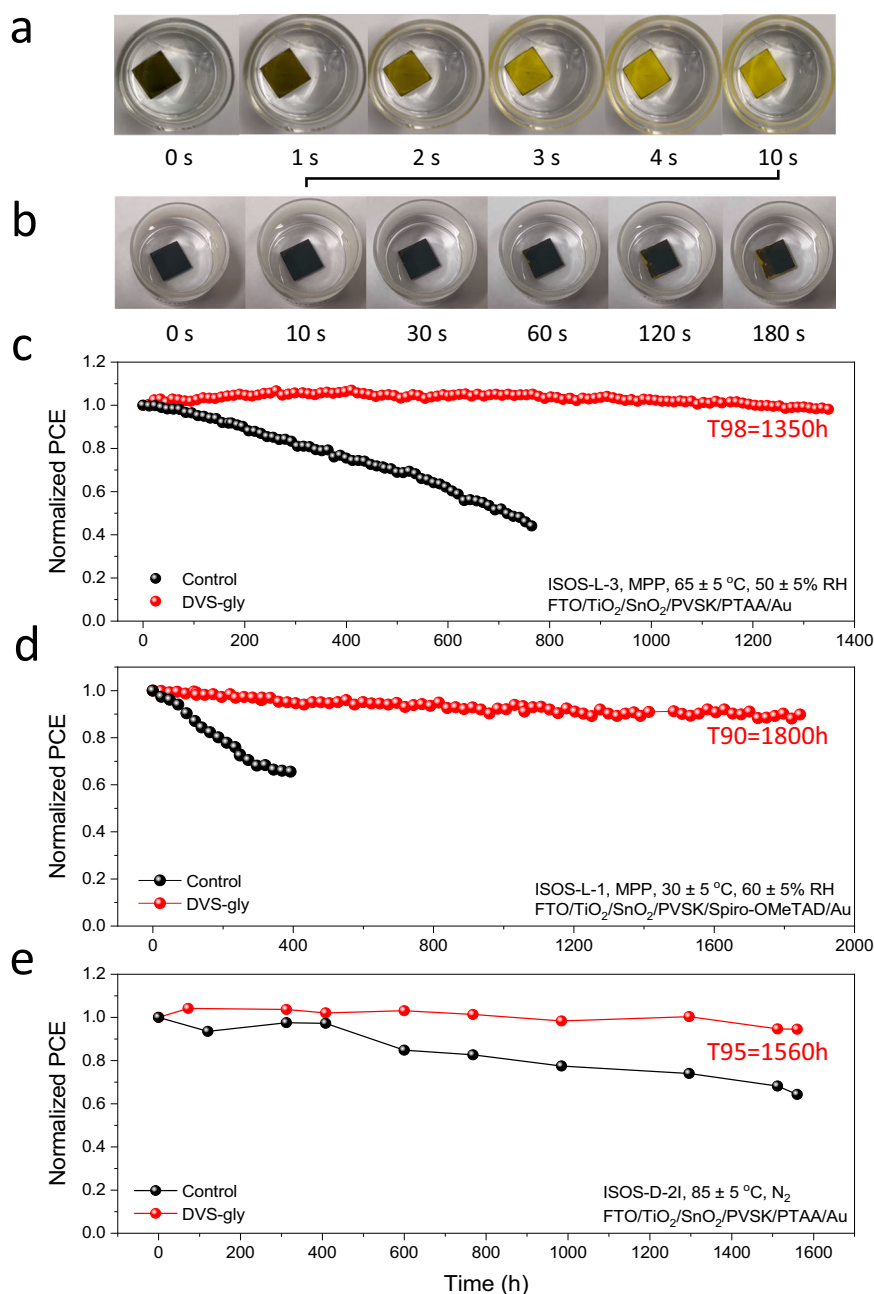
Table 1 | Photovoltaic parameters of the control, DVS-based, and DVS-gly-based PSCs under optimized conditions

Conditions	V$_{OC}$ (V)	J$_{SC}$ (mA cm^{-2})	FF (%)	PCE (%) Average	Best
Control (TiO$_2$ ETL)	1.165	25.18	79.22	23.03 ± 0.14	23.23
Control (TiO$_2$/SnO$_2$ QDs ETL)	1.200	25.21	79.77	23.66 ± 0.37	24.14
DVS	1.210	25.64	80.83	24.80 ± 0.22	25.08
DVS-gly	1.220	25.51	81.03	25.12 ± 0.07	25.22

Fig. 5 | Perovskite film water resistance and device stability. Images of (**a**) a control perovskite film and (**b**) a DVS-gly-based perovskite film directly immersed in water. **c**, **d** Long-term MPP tracking at elevated temperature (1-sun, 65 ± 5 °C, 50 ± 5% RH encapsulated devices: FTO/TiO$_2$/SnO$_2$/PVSK/PTAA/Au) and room temperature (1-sun, 30 ± 5 °C, 60 ± 5% RH, encapsulated devices: FTO/TiO$_2$/SnO$_2$/PVSK/spiro-OMeTAD/Au), respectively. **e** thermal stability (dark, 85 ± 5 °C, N$_2$, unencapsulated device: FTO/TiO$_2$/SnO$_2$/PVSK/PTAA/Au).

30 °C, respectively, which are significantly better than those of the control devices (Figs. 5c and d). Besides, we also evaluated the thermal stability of PSCs based on different HTLs, as shown in Fig. 5e and Supplementary Fig. 25a, respectively) in dark (ISOS-D-2I, 85 ± 5 °C, N$_2$). PTAA-based devices exhibit much prolonged thermal stability than spiro-OMeTAD, mainly due to the absence of metal ionic dopants. DVS-gly devices based on PTAA maintained over 95% of their initial PCE after 1560 h, which surpasses the control devices (only maintaining 64%), mainly attributed to the reduced tDOS at perovskite surface and GBs. DVS-gly devices also exhibit enhanced shelf stability under ambient atmosphere (25 ± 5 °C, 20 ± 5% RH, maintaining 98% of their initial PCE over 2300 h, as shown in Supplementary Fig. 25b). It's well known that shallow defects (with low migration activation energy) at

perovskite surface and grain boundaries initialize the permeation of moisture and oxygen into the perovskite films to accelerate the degradation of PSCs. The effective relief of shallow defects and improved moisture resistance through this strategy is responsible for enhanced stability under different aging conditions[35].

Discussion

This work provided an insightful strategy to synergically implement delicate perovskite crystallization manipulation and provide all-around protection at the perovskite surface and GBs during the pero[27]vskite forming process. The pre-embedded DVS dominated the FA-based intermediate transition during the delicate manipulation of perovskite crystallization and induced a three-dimensional

co-polymerization through nucleophiles post-treatment upon as-cast films. We validated that the polymer scaffold not only passivated the intrinsic defects at the perovskite surface and GBs but also released the residual strain at the near-surface region. We achieved high device performance with the lowest V_{OC} deficit among all perovskite systems. This strategy significantly improved the moisture resistance of perovskite films, and achieved much enhanced devices stability, which may advance the commercialization of this promising PV technology.

Methods

Materials
The following chemicals and solvents were used without further purification: lead iodide (PbI_2) (Sigma-Aldrich, 99.99%), lead(II) bromide ($PbBr_2$) (Sigma-Aldrich, 99.999%), formamidinium iodide (FAI) (Greatcell Energy), methylammonium bromide (MABr) (Greatcell Energy), and methylammonium chloride (MACl). All of the solvents were bought from Sigma-Aldrich, including Divinyl sulfone (contains 400-600 hydroquinone as inhibitor, $\geq$ 6%), dimethyl sulfoxide (DMSO), and N,N-dimethylformamide (DMF) (99.8%, anhydrous).

Device fabrication
FTO/glass substrates with laser patterns (sheet resistance $\approx$ 12 Ω per square) were cleaned in detergent, distilled water, acetone, and isopropanol, respectively. The FTO glass was submerged in a $TiCl_4$ solution at 70 °C for 60 minutes to produce the TiO_2 by employing the chemical bath deposition process. After that, the FTO substrate was repeatedly cleaned with distilled water and ethanol and dried for 30 minutes at 200 °C[36]. After 20 minutes of ultraviolet-ozone treatment, a thin coating of self-produced SnO_2 solution was spin-coated onto the previous TiO_2 layer for 30 seconds at 4000 rpm. Then, it was annealed for 60 mins at 200 °C in an ambient atmosphere. The mixed powders of FAI:MABr:MACl:$PbBr_2$:PbI_2 (molar ratio=1.41:0.04:0.4:0.04:1.47) in DMF/DMSO (4:1, v:v) were combined with appropriate amount of CsI mother solution (1.5 M, in DMSO) stock solution to create the $Cs_{0.03}(FA_{0.97}MA_{0.03})_{0.97}Pb(I_{0.97}Br_{0.03})_3$ perovskite precursor solution (bandgap = 1.53 eV). For the DVS-based perovskite ink, different amounts of DVS (0 to 20%, v:v) was incorporated into the perovskite solution in DMF. After the post-treatment of glycerol, the as-cast perovskite films were transferred into a controlled ambient environment (20%–30% relative humidity, RH) and annealed onto a hotplate at 120 °C for 60 mins to facilitate the spontaneous cross-linking and perovskite crystallization. The samples were transferred into the glovebox and spin-coated with BABr (2 mg/mL, IPA) and spiro-OMeTAD (80 mg/mL in CB, 29 μL of tBP, and 17.5 μL of Li-TFSI mother solution), respectively, followed by a 10 mins annealing at 100 °C. An 80 nm thick Au electrode was subsequently patterned by thermally evaporating on top of the device using a shadow mask.

Characterizations
Crystalline structure was explored on a Rigaku SmartLab X-ray diffractometer with Cu Kα radiation in a step of 0.01° and θ−2θ scan mode from 5° to 50°. Perovskite film morphology was examined by a high-resolution field emission scanning electron microscopy (SEM) (TESCAN VEGA3). Grazing-incidence wide-angle X-ray scattering (GIWAXS) was investigated using a Xeuss 2.0 SAXS/WAXS laboratory beamline with a Cu X-ray source (8.05 keV, 1.54 Å) and a Pilatus3R 300 K detector. The in-situ UV-vis absorption spectra were measured using an F20-UVX spectrometer (Filmetrics, Inc.) equipped with tungsten halogen and deuterium light sources. Appropriate amounts of FAI, DVS, and FAI/DVS were dissolved into DMSO-d6 to prepare the sample solutions. Their proton spectra were acquired using a 400 MHz NMR spectrometer. Steady-state photoluminescence (PL) and time-resolved decay spectra were measured using a PL spectrometer (Edinburgh Instruments, FLS920) with the excitation source of 636.2 nm picosecond pulsed diode laser (EPL-635, ~5 nJ/cm^2) and detected at 780 nm. TRPL decays spectra were fitted by the bi-exponential function: $I(t) = A_1 \exp(-\frac{t}{\tau_1}) + A_2 \exp(-\frac{t}{\tau_2})$ (1). Ultraviolet photoemission spectroscopy (UPS) measurement was carried out by a VG ESCLAB 220i-XL surface analysis system equipped with a mono-chromatic Al K X-ray source (1486.6 eV) in a vacuum of 3.0×10^{-8} Torr. For the completed devices, J-V curves were obtained using a Keithley 2400 Source Meter under standard AM 1.5 G illumination (Enli Technology Co. Ltd., Taiwan), and the light intensity was calibrated by a standard KG-5 Si diode. Both forward (from −0.2 to 1.25 V) and reverse scanning (from 1.25 to −0.2 V) were performed with a delay time of 100 ms. The test areas (0.04 cm^2) are typically defined by a metal mask with an aperture aligned with the active area. EQE spectra were measured with a QE-R 3011 EQE system (Enli Technology Co. Ltd., Taiwan) using 210 Hz chopped monochromatic light ranging from 300 to 850 nm. The EL EQE spectra were recorded by an LED photoluminescence quantum yield measurement system (Enli Tech LQ-100) equipped with the Keithley 2400 Source Measure Unit. The non-radiative recombination loss ($\Delta V_{OC,nr}$) can be derived from the EQE_{EL} at the injection current density equal to J_{SC} with the equation: $\Delta V_{OC, nr} = -\frac{k_B T}{q} \ln EQE_{EL}$ (2). Thermal admittance spectroscopy (TAS) was performed to estimate the energetic distribution of trap density within perovskite films under an AC voltage with the frequency decreased from 10^6 to 100 Hz according to the equations: $N_t(E_\omega) = -\frac{V_{bi}}{eW}\frac{dC}{d\omega}\frac{\omega}{k_B T}$ (3), $E_\omega = k_B T \ln\left(\frac{\beta T^2}{\omega}\right)$ (4), where V_{bi} is the built-in potential, W is the depletion width, C is the capacitance, ω is the applied angular frequency, and β is a temperature-independent parameter from the Arrhenius plot. V_{bi} and W could be calculated for a PSC device using the Mott-Schottky analysis.

Reporting summary
Further information on research design is available in the Nature Portfolio Reporting Summary linked to this article.

Data availability
All data generated or analyzed in this study are provided in the published article and its Supplementary Information. Source data are provided in this paper. Source data are provided with this paper.

References

1. Gratzel, M. The light and shade of perovskite solar cells. *Nat. Mater.* **13**, 838–842 (2014).
2. Green, M. A., Ho-Baillie, A. & Snaith, H. J. The emergence of perovskite solar cells. *Nat. Photonics* **8**, 506–514 (2014).
3. Chao, L. et al. Solvent Engineering of the Precursor Solution toward Large-Area Production of Perovskite Solar Cells. *Adv. Mater.* **33**, 2005410 (2021).
4. National Renewable Energy Laboratory (NREL) (2023). Best research-cell efficiency chart. https://www.nrel.gov/pv/assets/pdfs/best-research-cell-efficiencies.pdf.
5. Liu, K., Fong, P. W. K., Liang, Q. & Li, G. Upscaling perovskite solar cells via the ambient deposition of perovskite thin films. *Trends in Chemistry* **3**, 747–764 (2021).
6. Azmi, R. et al. Moisture-Resilient Perovskite Solar Cells for Enhanced Stability. *Adv. Mater.* e2211317 (2023).
7. Boyd, C. C., Cheacharoen, R., Leijtens, T. & McGehee, M. D. Understanding Degradation Mechanisms and Improving Stability of Perovskite Photovoltaics. *Chem. Rev.* **119**, 3418–3451 (2019).
8. Chen, B., Rudd, P. N., Yang, S., Yuan, Y. & Huang, J. Imperfections and their passivation in halide perovskite solar cells. *Chem. Soc. Rev.* **48**, 3842–3867 (2019).
9. Liu, C., Cheng, Y. B. & Ge, Z. Understanding of perovskite crystal growth and film formation in scalable deposition processes. *Chem. Soc. Rev.* **49**, 1653–1687 (2020).

10. Xiang, W. et al. Intermediate phase engineering of halide per-ovskites for photovoltaics. *Joule* **6**, 1–25 (2021).
11. Meng, W. et al. Revealing the strain-associated physical mechanisms impacting the performance and stability of perovskite solar cells. *Joule* **6**, 458–475 (2022).
12. Li, X. et al. In-situ cross-linking strategy for efficient and operationally stable methylammoniun lead iodide solar cells. *Nat. Commun.* **9**, 3806 (2018).
13. Luo, L. et al. Stabilization of 3D/2D perovskite heterostructures via inhibition of ion diffusion by cross-linked polymers for solar cells with improved performance. *Nat. Energy* **8**, 294–303 (2023).
14. Yang, M. et al. Reducing lead toxicity of perovskite solar cells with a built-in supramolecular complex. *Nature Sustain.* **6**, 1455–1464 (2023).
15. Yin, X. et al. Cross-Linking Polymerization Boosts the Performance of Perovskite Solar Cells: From Material Design to Performance Regulation. *Energy Environ. Sci.* **16**, 4251–4279 (2023).
16. Han, T. H. et al. Spontaneous Hybrid Cross-Linked Network Induced by Multifunctional Copolymer toward Mechanically Resilient Perovskite Solar Cells. *Adv. Funct. Mater.* **32**, 2207142 (2022).
17. Zheng, Z. et al. Pre-Buried Additive for Cross-Layer Modification in Flexible Perovskite Solar Cells with Efficiency Exceeding 22. *Adv. Mater.* **34**, e2109879 (2022).
18. Zhang, H. et al. Multifunctional Crosslinking-Enabled Strain-Regulating Crystallization for Stable, Efficient alpha-FAPbI3 -Based Perovskite Solar Cells. *Adv. Mater.* **33**, e2008487 (2021).
19. Duan, X. et al. Controlling Crystal Growth via an Autonomously Longitudinal Scaffold for Planar Perovskite Solar Cells. *Adv. Mater.*, e2000617 (2020).
20. Xia, R. et al. An Efficient Approach to Fabricate Air-Stable Perovskite Solar Cells via Addition of a Self-Polymerizing Ionic Liquid. *Adv. Mater.*, e2003801 (2020).
21. Hamill, J. C., Schwartz, J. & Loo, Y.-L. Influence of solvent coordination on hybrid organic–inorganic perovskite formation. *ACS Energy Lett.* **3**, 92–97 (2017).
22. Jiang, J., Vicent-Luna, J. M. & Tao, S. The role of solvents in the formation of methylammonium lead triiodide perovskite. *J. Energy Chem.* **68**, 393–400 (2022).
23. Huang, X. et al. Solvent racing crystallization: Low-solvation dispersion cosolvents for high-quality halide perovskites in photovoltaics. *Joule* **7**, 1556–1573 (2023).
24. Liang, Q. et al. Manipulating Crystallization Kinetics in High-Performance Blade-Coated Perovskite Solar Cells via Cosolvent-Assisted Phase Transition. *Adv. Mater.* **34**, 2200276 (2022).
25. Ahuja, S. K. et al. Fourier Transform Infrared (FTIR) Study of Thermal Stability in Vinylidene Fluoride Copolymers. *SPIE Fourier and Computerized Infrared Spectroscopy* **553**, 112–113 (1985).
26. Ellzy, M. W., Jensen, J. O. & Kay, J. G. Vibrational frequencies and structural determinations of di-vinyl sulfone. *Spectrochim Acta A Mol Biomol Spectrosc* **59**, 867–881 (2003).
27. del Agua, I. et al. DVS-Crosslinked PEDOT:PSS Free-Standing and Textile Electrodes toward Wearable Health Monitoring. *Adv. Mater. Technol.* **3**, 1700322 (2018).
28. Zhu, C. et al. Strain engineering in perovskite solar cells and its impacts on carrier dynamics. *Nat. Commun.* **10**, 815 (2019).
29. Liu, K. et al. Zwitterionic-surfactant-assisted room-temperature coating of efficient perovskite solar cells. *Joule* **4**, 2404–2425 (2020).
30. Fei, C. et al. Lead-chelating hole-transport layers for efficient and stable perovskite minimodules. *Science* **380**, 823–829 (2023).
31. Jiang, Q. et al. Surface passivation of perovskite film for efficient solar cells. *Nat. Photonics* **13**, 460–466 (2019).
32. Li, N. et al. Cation and anion immobilization through chemical bonding enhancement with fluorides for stable halide perovskite solar cells. *Nat. Energy* **4**, 408–415 (2019).
33. Ni, Z. et al. Evolution of defects during the degradation of metal halide perovskite solar cells under reverse bias and illumination. *Nat. Energy* **7**, 65–73 (2021).
34. Kim, H. S. et al. High efficiency solid-state sensitized solar cell-based on submicrometer rutile TiO2 nanorod and CH3NH3PbI3 perovskite sensitizer. *Nano Lett.* **13**, 2412–2417 (2013).
35. Ran, C., Xu, J., Gao, W., Huang, C. & Dou, S. Defects in metal triiodide perovskite materials towards high-performance solar cells: origin, impact, characterization, and engineering. *Chem. Soc. Rev.* **47**, 4581–4610 (2018).
36. Han, Y. et al. Controlled n-Doping in Air-Stable CsPbI2Br Perovskite Solar Cells with a Record Efficiency of 16.79%. *Adv. Funct. Mater.* **30**, 1909972 (2020).

Author contributions

G.L., Q.L., and K.L. conceived the idea. G.L., Y.Y., Q.L., and K.L. designed the experiments and analyzed the data. Y.H., Z.R., D.L. and L.C. helped to make the devices. H.X. and J. H. conducted NMR spectroscopy measurements and analysis. Z.W. assisted with PL and TRPL measurements. T.Z. helped with device encapsulation. C.Z. and Q.C. assisted with the GI-XRD analysis. Q.L., K.L., and P.W.K.F. carried out in-situ XRD and UV-vis absorption analysis. Q.L., K.L., Y.Y., and G.L. collaborated to prepare the manuscript. All authors discussed the results and commented on the manuscript.

Competing interests

The authors declare no competing interests.

Additional information

Supplementary information The online version contains supplementary material available at https://doi.org/10.1038/s41467-024-55414-4.

Correspondence and requests for materials should be addressed to Kuan Liu, Yang Yang or Gang Li.

Peer review information *Nature Communications* thanks Hyun Suk Jung, and the other, anonymous, reviewer(s) for their contribution to the peer review of this work. A peer review file is available.

Reprints and permissions information is available at http://www.nature.com/reprints